

A strong non-equilibrium bound for sorting of crosslinkers on growing biopolymers

Yuqing Qiu,^{1,2} Michael Nguyen,^{1,2} Glen M. Hocky,³ Aaron R. Dinner,^{1,2} and Suriyanarayanan Vaikuntanathan^{*1,2}

¹*James Franck Institute, University of Chicago, Chicago, IL*

²*Department of Chemistry, University of Chicago, Chicago, IL*

³*Department of Chemistry, New York University, New York, NY*

Understanding the role of non-equilibrium driving in self-organization is crucial for developing a predictive description of biological systems, yet it is impeded by their complexity. The actin cytoskeleton serves as a paradigm for how equilibrium and non-equilibrium forces combine to give rise to self-organization. Motivated by recent experiments that show that actin filament growth rates can tune the morphology of a growing actin bundle crosslinked by two competing types of actin binding proteins [Freedman et al. PNAS 116, 16192–16197 (2019)], we construct a minimal model for such a system and show that the dynamics are subject to a set of thermodynamic constraints that relate the non-equilibrium driving, bundle morphology, and molecular fluxes. The thermodynamic constraints reveal the importance of correlations between these molecular fluxes, and offer a route to estimating microscopic driving forces from microscopy experiments.

I. INTRODUCTION

Non-equilibrium driving is a crucial prerequisite for the function of many biological systems. Examples include kinetic proofreading [1–5], adaptation in molecular motors [6–8], and the suppression of phase decoherence in biochemical oscillators [9–14], among others. Given the ubiquitous role played by non-equilibrium driving in biology, much recent work has been focused on establishing the general tradeoffs between energy consumption and organization [15–20]. Here, motivated by recent experimental work [21–23], we consider growth and bundling dynamics of actin filaments and demonstrate that general energy-speed-morphology relations can be obtained for such systems.

The actin cytoskeleton harnesses chemical energy to perform mechanical work that enables cells to migrate, divide, and exert forces on their surroundings, among other functions [7, 24–28]. To perform these varied functions, a cell must be able to control the organization of its many components in both space and time. A growing body of evidence suggests that, surprisingly, much of this organization can arise due to passive competition between actin binding proteins (ABPs) [29]. At the same time, other processes such as the formation of a cytoskeletal ring require irreversible polymerization and motor activity [30, 31]. This suggests that cells can regulate their internal structures and, in turn, functions by tuning the relative contributions of passive and active processes. Support for this idea comes from recent *in vitro* experiments and simulations that demonstrate that the morphology of a growing actin bundle can be tuned not only by the binding affinities of the crosslinkers but also by the actin polymerization rates [22].

These observations, together with recent advances in non-equilibrium statistical mechanics [5, 9, 17, 32–34], raise the question whether the nonequilibrium driving—here due to polymerization—can be related to the emergent structure *quantitatively*. Here, we address this question and present a theoretical framework that bounds the

dynamics of a growing actin bundle. In particular, we derive constraints on a set of three matrices characterizing the process—a matrix containing the various non-equilibrium driving forces ($\delta\mu$, Eq. (11)), a matrix encoding the equilibrium and nonequilibrium morphologies (\mathbf{D} , Eq. (12)), and a matrix characterizing the covariance of the molecular fluxes (\mathbf{L}^{-1} , Section IV). For these three matrices, we show that

$$\text{Tr}\{\delta\mu - \mathbf{D} - \mathbf{L}^{-1}\} \geq 0, \text{Det}[\delta\mu - \mathbf{D} - \mathbf{L}^{-1}] \geq 0. \quad (1)$$

Eq. (1) has a flavor of the fluctuation dissipation relation. Indeed, when the equality is satisfied, Eq. (1) can be used to obtain a linear-response-like formula connecting the non-equilibrium forcing, the bundle morphology, and the response to fluctuations in molecular fluxes (Eq. (13)). Eq. (1) thus provides strong thermodynamic constraints on the non-equilibrium forcing, actin bundle morphology, and speed of growth. Notably, \mathbf{D} and \mathbf{L}^{-1} are experimentally accessible, such that Eq. (1) can be used to bound $\delta\mu$, which is not straightforward to measure directly.

In what follows, we first outline a minimal model that captures the salient features of actin polymerization and bundling and show that it captures the observations described above. We then proceed to derive our central results, and show how these thermodynamic uncertainty relations constrain the dynamics.

II. ACTIN POLYMERIZATION DRIVES SORTING OF ACTIN BUNDLING PROTEINS

Inspired by the experiments in Refs. 21 and 22, we consider a bundle consisting of two parallel actin filaments and two types of ABPs, α and β . The growth of a parallel actin bundle involves continuous actin monomer addition at one end, as well as continual binding and ‘zipping’ of the bundle by ABP binding at that same end. In the specific case shown in Fig. 1, α and β represent crosslinking proteins α -actinin and fascin, respectively, such that the bundles formed by the α ABPs are substantially more

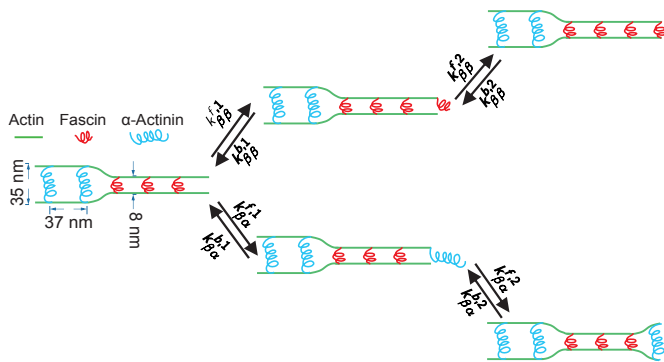


FIG. 1. Schematic of adding one ABP at the tip of a growing actin bundle. Here, α and β represent α -actinin and fascin, which are 35 nm and 8 nm in size, respectively. The energetic cost of bending actin disfavors the binding a fascin after an α -actinin, or *vice versa*, resulting in domains of consecutive α or β types of ABPs. $k_{ij}^{f,1}$ and $k_{ij}^{b,1}$ ($k_{ij}^{f,2}$ and $k_{ij}^{b,2}$) are the forward and backward rates for the first (second) site of an ABP binding, where i and j are the types of the last two ABPs at the tip; $k_{\alpha\alpha}^{f,1} = k_{\beta\alpha}^{f,1}$ because both rates represent the binding of the first site of an α ABP. An analogous schematic can be drawn for the case that the second-to-last ABP is α , and this case introduces four additional pairs of forward and backward rates with corresponding constraints.

widely spaced than those formed by the β ABPs. Consequently, the bending penalty of actin implicitly favors addition of the current crosslinker at the growing end, as it costs energy to switch from one type to the other. Under conditions of equilibrium, the cost of bending actin favors the formation of distinct domains of only α or β ABPs. In the case of *in vitro* experiments using an equimolar mixture of fluorescently labeled α -actinin and fascin binding to growing actin bundles, these domains are on the order of several micrometers (~ 100 crosslinkers) long [21]. As noted above, it has been reported [22] that the domain length statistics can be modulated by the rate of actin polymerization.

We construct a minimal model of this system with the following simplifications: first, we assume that the actin binding proteins can only bind and unbind from the sites at the leading edge and not from the bulk of the actin filament, and second, we assume that the two binding sites of each ABP bind sequentially and do not allow an ABP to bind to a single filament with both its sites. As a result, we need two pairs of forward rates $k_{ij}^{f,1}$ and backward rates $k_{ij}^{b,1}$ to describe the binding of first site of each ABP and two other pairs, $k_{ij}^{f,2}$ and $k_{ij}^{b,2}$, for their second site (Fig. 1). The consideration of both heads independently is more sophisticated than the kinetic Monte Carlo (KMC) models considered in Refs. 21 and 22 and is consistent with the experimental and simulation observations therein.

Here, we further decompose the forward rate of $k_{ij}^{f,m}$ into an equilibrium component, $k_{ij,eq}^{f,m}$, that satisfies a lo-

cal detailed balance rule and accounts for all the energetics associated with ABP binding and filament deformations, and a component $dk_{ij}^{f,m}$ that can model any non-equilibrium contributions to the rate,

$$k_{ij}^{f,m} = k_{ij,eq}^{f,m} dk_{ij}^{f,m}. \quad (2)$$

We assert that only the forward rates are modified by any non-equilibrium effects including actin polymerization and we set all the $k_{ij}^{b,m}$ to unity. The equilibrium factor $k_{ij,eq}^{f,m}$ accounts for the binding affinity of an ABP. In cases where an attached ABP binds to the second actin filament, this equilibrium part also accounts for the energy penalty associated with bending the actin filament if the newly bound ABP is different from the previous ABP at the tip (e.g., rate $k_{\beta\alpha,eq}^{f,2}$ in Fig. 1) and the free energy associated with zipping the actin bundle (e.g., rates $k_{\beta\beta,eq}^{f,2}$ and $k_{\beta\alpha,eq}^{f,2}$ in Fig. 1).

The non-equilibrium component in our model, $dk_{ij}^{f,m}$, heuristically accounts for any effects due to the finite rate of actin growth and polymerization, excess concentration or chemical potential of various ABPs in solution, and their molecular structure. Given this, we generically decompose the non-equilibrium components as

$$dk_{ij}^{f,m} = dk_j = 1 + f_{\text{molecular},j} f_{\text{density},j} f_{\text{pol},j} \quad (3)$$

where i and j are the types of ABPs at the bundle tip. The factor f_{pol} models the modulation of the rates due to the finite rate of growth of the actin filaments (k_{grow}). Specifically, over a time scale τ , the average increase in the number of binding sites on the filaments is $k_{\text{grow}}\tau$ and $k_{ij,eq}^{f,1}\tau$ is the number of binding events per binding site. Assuming Poisson statistics, the net rate of ABP binding is hence modulated by the factor,

$$f_{\text{pol},i} = 1 - e^{-k_{ii,eq}^{f,1} k_{\text{grow}} \tau^2} \quad (4)$$

The factor f_{pol} is essentially the probability of binding at least one ABP within time τ . f_{pol} increases from a value of 0 when k_{grow} is negligible to a value of 1 for rapid actin polymerization. It acts as a scaling factor that tunes the rates from their equilibrium values $k_{ij,eq}^{f,m}$ to their maximum rates.

The rates of ABP binding are also influenced by the ABP concentrations in solution around the actin filaments. The phenomenological factor f_{density} accounts for these effects. Finally, the phenomenological factor, $f_{\text{molecular}}$ has been introduced to account for any remaining kinetic differences between the ABPs. Such factors could modulate the maximum rates of adding ABPs in fast growing bundles, but they do not affect the equilibrium rates $k_{ij,eq}^{f,m}$ and the corresponding equilibrium structure of the bundle [22].

KMC simulations of this minimal model (described in SI Sec. S1) reproduce the crossover of domain lengths in fast growing actin bundles (Fig. 2) [22]. It thus captures the essential physics of the system and serves as a

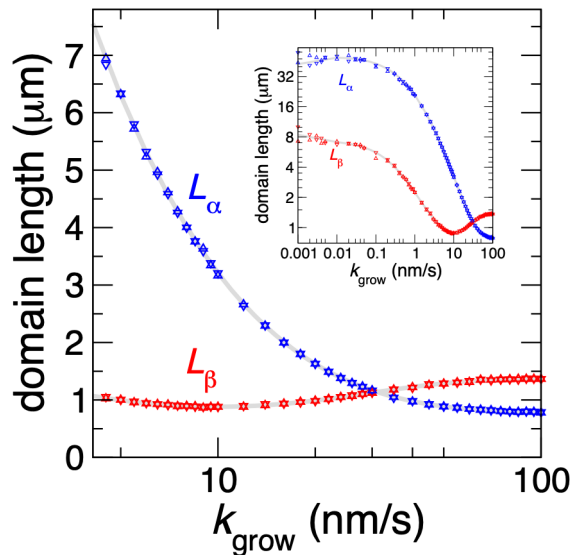


FIG. 2. Domain length of α and β ABPs as a function of polymerization rate k_{grow} . The distance between neighboring ABPs is assumed to be $0.037 \mu\text{m}$ in computing domain lengths [21]. Blue and red triangles are domain lengths L_α and L_β measured from KMC simulations. Up and down triangles represent the domain lengths measured in simulations with initial configurations composed of either all α or all β types of ABPs, respectively. Gray lines (Eq. (S15)) are the domain lengths computed by self-consistently solving the master equation (Eq. (5)). The parameters for both KMC simulations and the master equation are $k_{\alpha\alpha,eq}^{f,1} = 6$, $k_{\beta\beta,eq}^{f,1} = 2$, $f_{\text{density},\alpha} = f_{\text{density},\beta} = 100$, $f_{\text{molecular},\alpha} = 0.4$, $f_{\text{molecular},\beta} = 1$, $L_{\alpha,eq} = 900(33.3\mu\text{m})$, $L_{\beta,eq} = 300(11.1\mu\text{m})$ and $\tau = 1\text{s}$. The inset shows the domain lengths over a wider range of polymerization rates with the same symbols. The plateaus toward the left of the inset represent the domain lengths approaching their equilibrium values.

meaningful starting point for development of a theoretical framework that shows that the behavior is bounded by a general energy-speed-morphology relation.

III. CONNECTIONS BETWEEN THE GROWTH AND MORPHOLOGY OF ACTIN BUNDLES: A MARKOV STATE MODEL

The number of accessible states of the Markov chain for actin polymerization and bundling, as defined in the last section, grows rapidly as a function of time. Writing down thermodynamic relations for such growing systems becomes cumbersome. Here, we show that it is in fact possible to account for the behavior of the growing system using only a tractable, finite-state, Markov model. Using this model, we derive thermodynamic bounds for the non-equilibrium sorting process in Fig. 3.

We begin by introducing a mean-field treatment for the various configurations that arise at the tip as ABPs associate and dissociate sequentially (Fig. 3). The forward

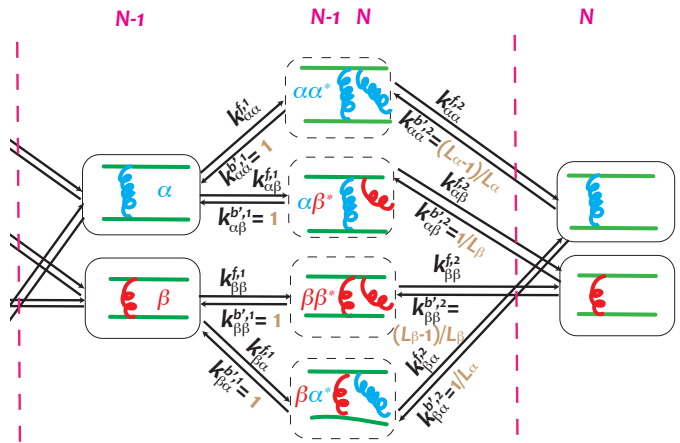


FIG. 3. Schematic of the N^{th} cross-linker binds to the actin pairs. The states between two pink dashed lines describe the N^{th} ABP binding. Arrows link states between which the transitions are allowed. $k_{ij}^{f,m}$ and $k_{ij}^{b,m}$ are the forward and backward rates, where i and j are the types of the last two ABPs at the tip and $*$ represents a half bound state. The rates used in the KMC simulations and in the master equation are compared in Table S1.

rates $k_{ij}^{f,m}$ are consistent with those used in KMC simulations, accounting for the energetic terms in binding ABPs and the effect of actin polymerization. The backward rates in the finite-state model self-consistently account for the probability of finding the appropriate ABP in the bulk of the actin bundle. For instance, using L_α to denote the domain lengths of α type ABPs and L_β for its β counterpart, the probability of finding an $\alpha\alpha^*$ configuration (where $*$ stands for half bound state as in Fig. 3) during unbinding one head of the last α ABP is $(L_\alpha - 1)/L_\alpha$ and the probability of finding a $\beta\alpha^*$ configuration is $1/L_\alpha$. In computing the unbinding rate $k_{ij}^{b',m}$ used in the finite-state model, we multiply the backward rates $k_{ij}^{b,m}$ in KMC simulations by the corresponding conditional probabilities. Note that the effective backward rate for unbinding the first head of an ABP, $k_{ij}^{b',1}$, is equal to $k_{ij}^{b,1}$ in KMC simulations because the conditional probabilities in these transitions are 1. The difference in $k_{ij}^{b',1}$ and $k_{ij}^{b',2}$ is because the unbinding of an ABP's first site $k_{ij}^{b',1}$ initiates from state ij^* and reaches state i , so the type of the preceding ABP is known from the current state, while the unbinding of ABP's second site $k_{ij}^{b',2}$ initiates from state j and the type of the preceding ABP i is uncertain (see Fig. 3). We confirm the expressions of these conditional probabilities by extracting the effective backward rates and domain length ratios from the full KMC simulations (Fig. S1).

Given these expressions for the rates, we can write a master equation describing the evolution of probabilities

of the various *tip* configurations, P_{ij} :

$$WP = \sum_{i,j=\alpha,\beta} (k_{ij}^{f,1} P_i - k_{ij}^{b',1} P_{ij*}) + k_{ij}^{f,2} P_{ij*} - k_{ij}^{b',2} P_j = 0. \quad (5)$$

However, this master equation depends on the average domain length L_α and L_β . To solve the master equation of this system and get closed form expressions of P_{ij} at the steady state, we require a relation that connects the tip configuration probabilities to the domain lengths. Such a connection can be obtained by noting that as the bundle barbed end grows, the tip configuration merges into the bulk of the bundle. The probabilities of tip configurations at steady state together with their corresponding rates determine the relative amounts of the two types of ABPs growing into the bulk. In other words, the fluxes $J_{N-1,i,N,j} = k_{ij}^{f,1} P_i - k_{ij}^{b',1} P_{ij*} = k_{ij}^{f,2} P_{ij*} - k_{ij}^{b',2} P_j$ are proportional to the probabilities of sampling the corresponding ABPs in the bulk (see Eq. (S13)).

Indeed, this reasoning can be put on a firm mathematical footing by adapting the calculations in Ref. 35. Specifically, as described in SI Section S2, we derive self-consistency conditions that relate the currents at which various tip configurations grow to the domain lengths in bulk:

$$\begin{aligned} J_{N-1,\alpha,N,\alpha} &= \frac{L_\alpha - 1}{L_{\text{tot}}} J_{\text{tot}} \\ J_{N-1,\beta,N,\beta} &= \frac{L_\beta - 1}{L_{\text{tot}}} J_{\text{tot}} \\ J_{N-1,\alpha,N,\beta} &= J_{N-1,\beta,N,\alpha} = \frac{1}{L_{\text{tot}}} J_{\text{tot}} \end{aligned} \quad (6)$$

where $N-1, i, N, j$ denotes the tip configurations at position $N-1$ and N , J_{tot} is the sum of the four currents, and $L_{\text{tot}} \equiv L_\alpha + L_\beta$. We measure the currents and domain lengths from KMC simulations, and Fig. S2 demonstrates the validity of the relations between the fluxes and domain lengths in Eq. (6).

The master equation (Eq. (5)) can now be solved with these additional self-consistency conditions. Expressions for the non-equilibrium domain lengths L_α and L_β can also be readily obtained (Eq. (S15)). The gray lines in Fig. 2 illustrate that these predictions are in excellent agreement with the domain lengths in KMC simulations for the full range of actin polymerization rates. This model also recovers the trend shown previously by simulations [22] that as the binding affinity of the short crosslinker (equivalent to β ABP in our model) is weakened, the crossover of domain lengths is deferred to a faster growth speed. Thus our mean-field treatment is able to capture the behavior of the model quantitatively.

IV. THERMODYNAMIC CONSTRAINTS BETWEEN THE NON-EQUILIBRIUM FORCING, FLUCTUATIONS, AND MORPHOLOGY

The non-equilibrium thermodynamics of the growing actin bundle can now be probed. Using the master equation (Eq. (5)) and the finite-state Markov model in Fig. 3, the entropy production rate $\dot{\sigma}$ for our effective Markov model can be written as

$$\dot{\sigma} = J_{\text{tot}}(\Delta\mu - \varepsilon_{\text{diss}}) \geq 0. \quad (7)$$

The factor $\Delta\mu$ represents the non-equilibrium forces driving polymerization; it is defined as

$$\Delta\mu = \frac{2}{L_{\text{tot}}} \left(\sum_i^{\alpha,\beta} L_i \log dk_i \right). \quad (8)$$

The factor $\varepsilon_{\text{diss}}$ is a measure of the difference between the non-equilibrium and equilibrium morphologies as characterized by the respective average domain lengths $L_{\beta,\text{eq}}$ and $L_{\alpha,\text{eq}}$.

$$\begin{aligned} \varepsilon_{\text{diss}} &= -\frac{1}{L_{\text{tot}}} \left(\sum_i^{\alpha,\beta} L_i \log \frac{L_i}{L_{i,\text{eq}}} \right. \\ &\quad \left. - \sum_i^{\alpha,\beta} (L_i - 1) \log \frac{L_i - 1}{L_{i,\text{eq}} - 1} \right). \end{aligned} \quad (9)$$

Eq. (7) is a statement of the second law of thermodynamics. However, we can improve on this bound substantially by adapting recent work [36, 37]. Specifically, we show in the SI Section. S3 that a stronger matrix relation can be obtained that is valid far from equilibrium. This is our main result, Eq. (1), which we reproduce here for convenience:

$$\text{Tr}\{\delta\boldsymbol{\mu} - \mathbf{D} - \mathbf{L}^{-1}\} \geq 0, \text{Det}[\delta\boldsymbol{\mu} - \mathbf{D} - \mathbf{L}^{-1}] \geq 0. \quad (10)$$

We now define the matrices $\delta\boldsymbol{\mu}$, \mathbf{D} and \mathbf{L}^{-1} precisely. The matrix $\delta\boldsymbol{\mu}$ depends on the non-equilibrium driving forces $\delta\mu_{\alpha/\beta} \equiv \log dk_{\alpha/\beta}$ in Eq. (3) and the average non-equilibrium domain lengths $L_{\alpha/\beta}$:

$$\delta\boldsymbol{\mu} = \begin{pmatrix} \delta\mu_\alpha \gamma_1^\alpha + \delta\mu_\beta \gamma_2^\beta & \delta\mu_\alpha \gamma_3^\alpha + \delta\mu_\beta \gamma_3^\beta \\ \delta\mu_\alpha \gamma_3^\alpha + \delta\mu_\beta \gamma_3^\beta & \delta\mu_\alpha \gamma_2^\alpha + \delta\mu_\beta \gamma_1^\beta \end{pmatrix} \quad (11)$$

where $\gamma_1^{\alpha/\beta} \equiv [(L_{\text{tot}} - 1)^2 / (L_{\alpha/\beta} - 1) + 1] / L_{\text{tot}}$, $\gamma_2^{\alpha/\beta} \equiv [1 / (L_{\alpha/\beta} - 1) + 1] / L_{\text{tot}}$, and $\gamma_3^{\alpha/\beta} \equiv -L_{\beta/\alpha} / [L_{\text{tot}} (L_{\alpha/\beta} - 1)]$. The matrix \mathbf{D} depends on the non-equilibrium and equilibrium domain lengths of ABPs and is defined as

$$\mathbf{D} = \begin{pmatrix} dp_\alpha \gamma_1^\alpha + dp_\beta \gamma_2^\beta + \epsilon & dp_\alpha \gamma_3^\alpha + dp_\beta \gamma_3^\beta + \epsilon \\ dp_\alpha \gamma_3^\alpha + dp_\beta \gamma_3^\beta + \epsilon & dp_\alpha \gamma_2^\alpha + dp_\beta \gamma_1^\beta + \epsilon \end{pmatrix} \quad (12)$$

where $dp_{\alpha/\beta} \equiv (1/2)(\ln[(L_{\alpha/\beta} - 1)/L_{\alpha/\beta}] - \ln[(L_{\alpha/\beta}^{\text{eq}} - 1)/L_{\alpha/\beta}^{\text{eq}}])$ and $\epsilon \equiv (1/(2L_{\text{tot}}))(\ln[(L_\alpha^{\text{eq}} - 1)/(L_\alpha - 1)] +$

$\ln[(L_\beta^{\text{eq}} - 1)/(L_\beta - 1)]$). The \mathbf{D} matrix only depends on the equilibrium and non-equilibrium morphologies of the bundle. \mathbf{L}^{-1} is proportional to the inverse of the covariance matrix of fluxes and is computed as $\mathbf{L}^{-1} \equiv \lim_{t \rightarrow \infty} J_{\text{tot}} \mathbf{M}^{-1}/t$, in which \mathbf{M} has the elements $M_{ij} = \langle \delta J_i \delta J_j \rangle$ and t is the time of growth. In Fig. 4, we numerically verify Eq. (1)/Eq. (10) for various parameter combinations.

The equality in Eq. (10) holds only when $\delta\boldsymbol{\mu} - \mathbf{D} = \mathbf{L}^{-1}$. In that case multiplying Eq. 1 by the column vector \mathbf{J} , containing the the average fluxes $J_{\alpha/\beta}$ computed using Eq. (6) as $J_{\alpha/\beta} = J_{N-1,\alpha,N,\alpha/\beta} + J_{N-1,\beta,N,\alpha/\beta}$ (detailed in SI Section. S4), we readily obtain

$$\mathbf{dk} - \mathbf{D}[\mathbf{p}] = \tilde{\mathbf{L}}^{-1} \cdot \mathbf{J} \quad (13)$$

where $\tilde{\mathbf{L}}^{-1} \equiv \mathbf{L}^{-1}/J_{\text{tot}}$, \mathbf{dk} is a column vector with elements $\log dk_{\alpha/\beta}$ (Eq. (3)), and $\mathbf{D}[\mathbf{p}]$ is a column vector with elements that are the relative entropies between the equilibrium and non-equilibrium domain morphologies of the two crosslinkers in the bundle (Eqs. (S32) and (S33)).

Eq. (13) can be viewed as an extension of the fluctuation dissipation relation to our non-equilibrium bundling and polymerization process. It relates the various driving forces \mathbf{dk} and a relative entropic measure of the distance between the non-equilibrium and equilibrium structures, $\mathbf{D}[\mathbf{p}]$, to the various observed fluxes \mathbf{J} through the flux covariance matrix $\tilde{\mathbf{L}}^{-1}$.

The so called thermodynamic uncertainty relations (TUR) [33, 34, 36–38] can also be readily derived from Eq. (10). Specifically, Eq. (10) implies that $\tilde{\mathbf{J}}^T \cdot [\delta\boldsymbol{\mu} - \mathbf{D} - \mathbf{L}^{-1}] \cdot \tilde{\mathbf{J}} \geq 0$ for any vector $\tilde{\mathbf{J}}$. Hence, the so called multidimensional thermodynamic relation (MTUR) [37] can be derived (SI Section S5):

$$J_{\text{tot}}(\Delta\mu - \varepsilon_{\text{diss}}) = 2\mathbf{J}^T \cdot (\mathbf{dk} - \mathbf{D}[\mathbf{p}]) \geq 2\mathbf{J}^T \cdot \tilde{\mathbf{L}}^{-1} \mathbf{J}. \quad (14)$$

Our central result provides a connection between the microscopic driving forces represented by $\delta\boldsymbol{\mu}$ or \mathbf{dk} , the non-equilibrium structure of the bundle as encoded by matrix \mathbf{D} or $\mathbf{D}[\mathbf{p}]$, and the fluctuations of the various fluxes denoted by \mathbf{L}^{-1} (obtained in the non-equilibrium steady state). Experimentally, it is possible to measure the fluxes of various bundling proteins, and the structure of the bundles. Then, one can use Eq. (1) to bound the microscopic driving forces. These microscopic forces generally cannot be measured directly. Further, in non-equilibrium regimes where the \mathbf{L}^{-1} matrix exhibits singular or close to singular behavior, our results suggest that the system might be insensitive to perturbations that tune the various microscopic driving forces, \mathbf{dk} . Our results suggest that the non-equilibrium bundling morphology can be effectively tuned away from such points.

Finally, Eq. (1)/Eq. (10) can also be used to assess the relative importance of accounting for the statistics of the individual fluxes. To do so, we use the thermodynamic uncertainty relations to derive a bound for the rate of

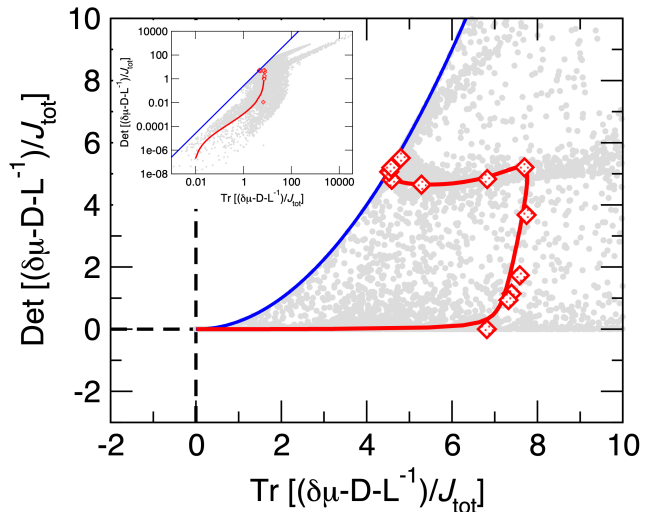


FIG. 4. Numerical verification of Eq. (10). The blue boundary marks the location of the inequality $\text{Tr}[\mathbf{M}] \geq 2\sqrt{\text{Det}[\mathbf{M}]}$ for a two dimensional square matrix \mathbf{M} . The red diamonds are results from the non-equilibrium KMC simulations with the parameters used in Fig. 2 and the red line is the theoretical mean field prediction for those same parameters. Gray dots are computed by constructing the matrices $\delta\boldsymbol{\mu}$, \mathbf{D} , and \mathbf{L}^{-1} using the master equation results and computing the eigenvalues of $(\delta\boldsymbol{\mu} - \mathbf{D} - \mathbf{L}^{-1})/J_{\text{tot}}$ using Mathematica [39] for randomly selected parameters from $L_{\beta,\text{eq}} = [1, 90000]$, $f_{\text{density},\beta} = [1, 100]$ and $k_{\text{grow}} = [0.001, 100]$ nm/s, with all other parameters the same as the red line. The inset shows these two quantities for a wider range, with both axes in logarithmic scale. We do not consider $k_{\text{grow}} < 0.001$ nm/s due to limitations of numerical precision. Eq. (1)/Eq. (10) provides strong constraints between the non-equilibrium forcing, morphology, and speed of growth.

entropy production in terms of the total flux, J_{tot} :

$$\Delta\mu \geq \varepsilon_{\text{diss}} + \frac{2\langle J_{\text{tot}} \rangle}{t\langle \delta J_{\text{tot}}^2 \rangle}. \quad (15)$$

Here, t is the growth time of the bundle, $\langle J_{\text{tot}} \rangle$ is the average total flux of adding ABPs to the bundle, and $\langle \delta J_{\text{tot}}^2 \rangle$ is its variance. In Fig. 5, we compare the performance of Eq. (15) (brown) with that of Eq. (7) (blue). We see that the TUR bound is closer to the real driving $\Delta\mu$ compared with the second-law bound. Nevertheless, it still fails significantly at $k_{\text{grow}} \approx 1$ nm/s, where it only recovers about 6% of the actual driving. This implies that controlling the overall kinetics is not enough for facilitating the sorting of ABPs.

In Fig. 5, we also plot the MTUR bound (Eq. (14)) using cumulants of fluctuations in the individual fluxes from KMC simulations. Although not perfect, this bound recovers at least 46% of the actual driving $\Delta\mu$ for the full range of polymerization rates. The increasing gap between the MTUR bound and the actual driving is consistent with our central result in Fig. 4 that $\text{Tr}[\delta\boldsymbol{\mu} - \mathbf{D} - \mathbf{L}^{-1}]$ becomes further away from zero as microscopic driving

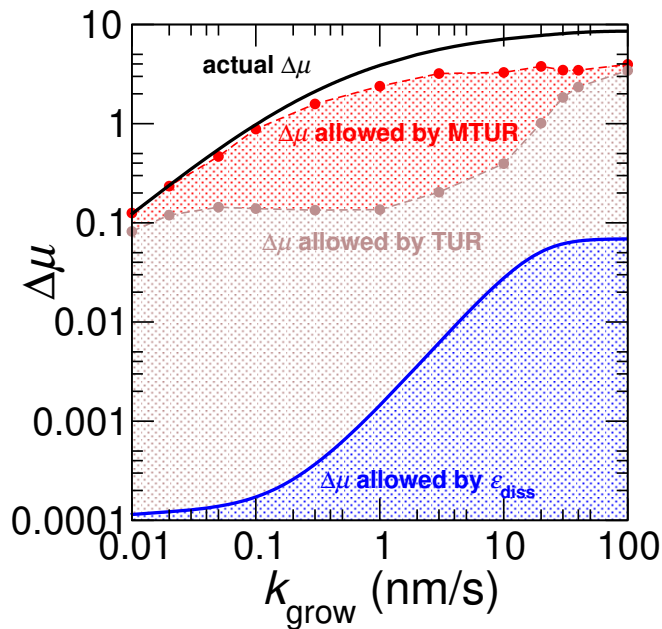


FIG. 5. Comparison of bounds on the non-equilibrium driving force $\Delta\mu$. The black line (Eq. (8)) is the actual driving force predicted by the master equation. The blue curve (Eq. (7)) is the driving force required for morphology change. The brown (Eq. (15)) and red (Eq. (14)) lines are the thermodynamic bounds computed from KMC simulations using TUR and MTUR. Each of the brown and red data points is generated with 500 independent KMC simulations, each of 10^7 steps. All parameters of the KMC simulations are the same as in Fig. 2.

becomes stronger and makes growth faster.

The MTUR bound in Eq. (14) is equivalent to considering a scalar observable $J_\phi = \cos \phi J_\alpha + \sin \phi J_\beta$ and then maximizing $2 \langle J_\phi \rangle^2 / (t J_{\text{tot}} \langle \delta J_\phi^2 \rangle)$ by varying ϕ (SI Section S5). When $\tan \phi = 1$, we recover the TUR bound in Eq. (15). Compared with this TUR bound, we find that the MTUR bound is mostly improved where the optimized $\tan \phi$ values deviate significantly from 1 (Fig. S4), and the fluxes are strongly correlated. Hence it is crucial to take into consideration the statistics of the individual fluxes. Indeed, the analytical expression of $\tan \phi$ (Eq. (S41)) and the empirical results in Fig. S5 and Fig. S6 show that $\tan \phi$ is mainly governed by the ratio of the domain lengths, L_α/L_β . In the regime $k_{\text{grow}} \approx 0.1$ to 10 nm/s, the domain lengths of the two ABPs differ

significantly. We conclude that thermodynamic costs can be seriously masked if only the total flux instead of individual ones are resolved in regimes where the two ABPs display remarkably different sorting behavior.

V. CONCLUSIONS

In conclusion, we have derived a strong thermodynamic constraint relating the microscopic driving of a growing bundle (denoted by $\delta\mu$ in Eq. (1)), the morphology of the bundle in its non-equilibrium steady state as described by the matrix \mathbf{D} , and the statistics of the rates of incorporation of crosslinkers as described by the matrix \mathbf{L}^{-1} . Our central results, which can be viewed as extensions of the fluctuation dissipation relations, also have practical applications. As an example, they potentially provide a route to estimate microscopic driving forces (contained in the $\delta\mu$ matrix) from experiments in which the various fluxes and morphologies are measured using microscopy and quantitative image analysis

While this current work is focused exclusively on the growth dynamics of bundled actin networks, we anticipate that the formalism presented here can be used in other contexts, such as the interplay between structure, speed, and non-equilibrium forcing in the growth dynamics of branched actin networks [40–42], the self-organization of other ABPs to distinct actin network architectures (e.g. networks initiated by formin or the Arp2/3 complex) [29], and the sorting of ABPs to distinct networks under confinement [23].

VI. ACKNOWLEDGMENTS

This work was mainly supported by a DOE BES Grant DE-SC0019765 through funding to SV, YQ, MN. YQ was also supported by a Yen Fellowship and the University of Chicago Materials Research Science and Engineering Center, which is funded by National Science Foundation under award number DMR-2011854. MN was also supported by a NSF Graduate research fellowship. GMH was supported by National Institute of Health award R35 GM138312. ARD was supported by National Institute of Health award R35 GM136381. We thank Chatipat Lorpaboon for help with the AFINES simulation software. Simulations were performed on the Midway cluster of the University of Chicago Research Computing Center.

-
- [1] John J Hopfield. Kinetic proofreading: a new mechanism for reducing errors in biosynthetic processes requiring high specificity. *Proc. Natl. Acad. Sci.*, 71(10):4135–4139, 1974.
- [2] David Andrieux and Pierre Gaspard. Nonequilibrium generation of information in copolymerization processes. *Proc. Natl. Acad. Sci.*, 105(28):9516–21, July 2008.

- [3] Pablo Sartori and Simone Pigolotti. Thermodynamics of error correction. *Phys. Rev. X*, 5:041039, Dec 2015.
- [4] Jenny M. Poulton, Pieter Rein ten Wolde, and Thomas E. Ouldridge. Nonequilibrium correlations in minimal dynamical models of polymer copying. *Proc. Natl. Acad. Sci.*, 116(6):1946–1951, 2019.

- [5] Arvind Murugan, David A Huse, and Stanislas Leibler. Speed, dissipation, and error in kinetic proofreading. *Proc. Natl. Acad. Sci.*, 109(30):12034–12039, 2012.
- [6] Udo Seifert. Stochastic thermodynamics of single enzymes and molecular motors. *Eur. Phys. J. E*, 34(3):1–11, 2011.
- [7] Michael Murrell, Patrick W Oakes, Martin Lenz, and Margaret L Gardel. Forcing cells into shape: the mechanics of actomyosin contractility. *Nature reviews Molecular cell biology*, 16(8):486–498, 2015.
- [8] Sebastian Fürthauer, Bezia Lemma, Peter J Foster, Stephanie C Ems-McClung, Che-Hang Yu, Claire E Walczak, Zvonimir Dogic, Daniel J Needleman, and Michael J Shelley. Self-straining of actively crosslinked microtubule networks. *Nat. Phys.*, 15(12):1295–1300, 2019.
- [9] Ganhui Lan, Pablo Sartori, Silke Neumann, Victor Sourjik, and Yuhai Tu. The energy-speed-accuracy tradeoff in sensory adaptation. *Nat. Phys.*, 8(5):422–428, May 2012.
- [10] Chenyi Fei, Yuansheng Cao, Qi Ouyang, and Yuhai Tu. Design principles for enhancing phase sensitivity and suppressing phase fluctuations simultaneously in biochemical oscillatory systems. *Nat. Commun.*, 9(1):1–10, 2018.
- [11] Yuansheng Cao, Hongli Wang, Qi Ouyang, and Yuhai Tu. The free-energy cost of accurate biochemical oscillations. *Nat. Phys.*, 11(9):772–778, 2015.
- [12] Samuel J Bryant and Benjamin B Machta. Energy dissipation bounds for autonomous thermodynamic cycles. *Proc. Natl. Acad. Sci.*, 117(7):3478–3483, 2020.
- [13] Clara del Junco and Suriyanarayanan Vaikuntanathan. High chemical affinity increases the robustness of biochemical oscillations. *Phys. Rev. E*, 101(1):012410, 2020.
- [14] Clara del Junco and Suriyanarayanan Vaikuntanathan. Robust oscillations in multi-cyclic markov state models of biochemical clocks. *J. Chem. Phys.*, 152(5):055101, 2020.
- [15] A. Joshi, E. Putzig, A. Baskaran, and M. Hagan. The interplay between activity and filament flexibility determines the emergent properties of active nematics. *ArXiv e-prints*, 2017.
- [16] Jie Zhang, Erik Luijten, Bartosz A. Grzybowski, and Steve Granick. Active colloids with collective mobility status and research opportunities. *Chem. Soc. Rev.*, 46(18):5551–5569, sep 2017.
- [17] Laura Tociu, Étienne Fodor, Takahiro Nemoto, and Suriyanarayanan Vaikuntanathan. How dissipation constrains fluctuations in nonequilibrium liquids: Diffusion, structure, and biased interactions. *Phys. Rev. X*, 9:041026, Nov 2019.
- [18] Étienne Fodor, Takahiro Nemoto, and Suriyanarayanan Vaikuntanathan. Dissipation controls transport and phase transitions in active fluids: mobility, diffusion and biased ensembles. *New J Phys.*, 22(1):013052, 2020.
- [19] Michael Nguyen and Suriyanarayanan Vaikuntanathan. Design principles for nonequilibrium self-assembly. *Proc. Natl. Acad. Sci.*, 113(50):14231–14236, 2016.
- [20] Trevor GrandPre, Katherine Klymko, Kranthi K Mandadapu, and David T Limmer. Entropy production fluctuations encode collective behavior in active matter. *arXiv preprint arXiv:2007.12149*, 2020.
- [21] Jonathan D. Winkelman, Cristian Suarez, Glen M. Hocky, Alyssa J. Harker, Alisha N. Morganthaler, Jenna R. Christensen, Gregory A. Voth, James R. Bar-
tles, and David R. Kovar. Fascin- and α -actinin-bundled networks contain intrinsic structural features that drive protein sorting. *Curr. Biol*, 26(20):2697 – 2706, 2016.
- [22] Simon L Freedman, Cristian Suarez, Jonathan D Winkelman, David R Kovar, Gregory A Voth, Aaron R Dinner, and Glen M Hocky. Mechanical and kinetic factors drive sorting of f-actin cross-linkers on bundles. *Proc. Natl. Acad. Sci.*, 116(33):16192–16197, 2019.
- [23] Yashar Bashirzadeh, Steven A Redford, Chatipat Lorpai boon, Alessandro Groaz, Thomas Litschel, Petra Schwille, Glen M Hocky, Aaron R Dinner, and Allen P Liu. Actin crosslinker competition and sorting drive emergent guv size-dependent actin network architecture. *bioRxiv*, 2020.
- [24] Alexander Mogilner and George Oster. Cell motility driven by actin polymerization. *Biophys. J*, 71(6):3030–3045, 1996.
- [25] Richard B Dickinson. Models for actin polymerization motors. *Journal Math. Biol.*, 58(1-2):81, 2009.
- [26] Antoine Jégou and Guillaume Romet-Lemonne. Mechanically tuning actin filaments to modulate the action of actin-binding proteins. *Curr. Opin. Cell Biol.*, 68:72–80.
- [27] Margaret L Gardel, Ian C Schneider, Yvonne Aratyn-Schaus, and Clare M Waterman. Mechanical integration of actin and adhesion dynamics in cell migration. *Annu. Rev. Cell Dev. Bio.*, 26:315–333, 2010.
- [28] Sadanori Watanabe, Yoshikazu Ando, Shingo Yasuda, Hiroshi Hosoya, Naoki Watanabe, Toshimasa Ishizaki, and Shuh Narumiya. *mdia2* induces the actin scaffold for the contractile ring and stabilizes its position during cytokinesis in nih 3t3 cells. *Mol. Biol. Cell.*, 19(5):2328–2338, 2008.
- [29] Rachel S Kadzik, Kaitlin E Homa, and David R Kovar. F-actin cytoskeleton network self-organization through competition and cooperation. *Annu. Rev. Cell. Dev. Biol.*, 36:35–60, 2020.
- [30] Dimitrios Vavylonis, Jian-Qiu Wu, Steven Hao, Ben O’Shaughnessy, and Thomas D Pollard. Assembly mechanism of the contractile ring for cytokinesis by fission yeast. *Science*, 319(5859):97–100, 2008.
- [31] Dennis Zimmermann, Kaitlin E Homa, Glen M Hocky, Luther W Pollard, M Enrique, Gregory A Voth, Kathleen M Trybus, and David R Kovar. Mechanoregulated inhibition of formin facilitates contractile actomyosin ring assembly. *Nature Comm.*, 8(1):1–13, 2017.
- [32] Yuhai Tu. The nonequilibrium mechanism for ultrasensitivity in a biological switch: sensing by Maxwell’s demons. *Proc. Natl. Acad. Sci.*, 105(33):11737–41, August 2008.
- [33] Andre C Barato and Udo Seifert. Thermodynamic uncertainty relation for biomolecular processes. *Phys. Rev. Lett.*, 114(15):158101, 2015.
- [34] Todd R. Gingrich, Jordan M. Horowitz, Nikolay Perunov, and Jeremy L. England. Dissipation bounds all steady-state current fluctuations. *Phys. Rev. Lett.*, 116(12):120601, 2016.
- [35] Pierre Gaspard and David Andrieux. Kinetics and thermodynamics of first-order markov chain copolymerization. *J. Chem. Phys.*, 141(4):044908, 2014.
- [36] Jiawei Yan. Achievability of thermodynamic uncertainty relations, 2019.
- [37] Andreas Dechant. Multidimensional thermodynamic uncertainty relations. *J. Phys. A Math.*, 52(3):035001, 2018.

- [38] Jordan M Horowitz and Todd R Gingrich. Thermodynamic uncertainty relations constrain non-equilibrium fluctuations. *Nat. Phys.*, pages 1–6, 2019.
- [39] Wolfram Research, Inc. Mathematica, Version 12.2.
- [40] James Liman, Carlos Bueno, Yossi Eliaz, Nicholas P Schafer, M Neal Waxham, Peter G Wolynes, Herbert Levine, and Margaret S Cheung. The role of the Arp2/3 complex in shaping the dynamics and structures of branched actomyosin networks. *Proc. Natl. Acad. Sci.*, 117(20):10825–10831, 2020.
- [41] Peter Bieling, Julian Weichsel, Ryan McGorty, Pamela Jreij, Bo Huang, Daniel A Fletcher, R Dyche Mullins, et al. Force feedback controls motor activity and mechanical properties of self-assembling branched actin networks. *Cell*, 164(1-2):115–127, 2016.
- [42] Julian Weichsel and Ulrich S Schwarz. Two competing orientation patterns explain experimentally observed anomalies in growing actin networks. *Proc. Natl. Acad. Sci.*, 107(14):6304–6309, 2010.
- [43] Daniel T Gillespie. Exact stochastic simulation of coupled chemical reactions. *The journal of physical chemistry*, 81(25):2340–2361, 1977.
- [44] Richard S. Ellis. *Entropy, large deviations, and statistical mechanics*. Springer-Verlag, 1985.

SUPPORTING INFORMATION

S1. KINETIC MONTE CARLO (KMC) SIMULATIONS

We simulate the growth of an actin bundle with two types of ABPs using KMC simulations. Two initial configurations are selected for each simulation: an actin bundle composed of 100 α type ABPs or a bundle composed of 100 β type ABPs. We exclude this first 100 ABPs when measuring the final structure and find that domain lengths in the bundle are independent of its initial configuration in the parameter range we explore. For each step in the KMC simulations, we first identify which state the bundle tip is at, and all the possible forward and backward moves that can be initiated from this state. The KMC simulations are performed using the Gillespie algorithm [43]. We summarize the rates used in the KMC simulations in Table S1. To compute domain lengths in Fig. 2, we run one simulation of $S = 10^6$ steps at each k_{grow} and measure domain lengths L_α and L_β from the full bundle by counting the number of consecutive ABPs of the same type and averaging their lengths. To generate the KMC data points in Fig. 4 and Fig. 5, we run 500 simulations of $S = 10^6$ steps at each actin polymerization rate $k_{\text{grow}} > 0.01$ nm/s; at $k_{\text{grow}} = 0.01$ nm/s, we run 5000 simulations of $S = 2 \times 10^8$ steps to ensure the convergence of the covariance of the fluxes.

S2. MEAN FIELD MASTER EQUATION

A. The backward rates in the master equation account for conditional probabilities during unbinding

We summarize the rates used in the master equation in Table S1. While in the KMC simulations the backward rates are unity, in the master equation they include the conditional probabilities of finding the appropriate type of ABP during unbinding. We thus express them in terms of the domain lengths in the bulk. To validate these expressions, we compute the effective backward rates in KMC simulations by counting the number of occurrences of each unbinding case. Fig. S1 demonstrates that the expressions are quantitatively accurate.

TABLE S1. Forward and Backward rates for ABP in Master Equation(ME) and KMC Simulations

	Forward Rates	ME and KMC	Backward Rates(ME)	ME	Backward Rates(KMC)	KMC
First head of ABP	$k_{\alpha\alpha}^{f,1}$	$k_{\alpha\alpha}^{f,1} = k_{\beta\alpha}^{f,1}$	$k_{\alpha\alpha}^{b',1}$	1	$k_{\alpha\alpha}^{b,1}$	1
	$k_{\alpha\beta}^{f,1}$		$k_{\alpha\beta}^{b',1}$	1	$k_{\alpha\beta}^{b,1}$	1
	$k_{\beta\beta}^{f,1}$	$k_{\beta\beta}^{f,1} = k_{\alpha\beta}^{f,1}$	$k_{\beta\beta}^{b',1}$	1	$k_{\beta\beta}^{b,1}$	1
	$k_{\beta\alpha}^{f,1}$		$k_{\beta\alpha}^{b',1}$	1	$k_{\beta\alpha}^{b,1}$	1
Second head of ABP	$k_{\alpha\alpha}^{f,2}$		$k_{\alpha\alpha}^{b',2}$	$(L_\alpha - 1)/L_\alpha$	$k_{\alpha\alpha}^{b,2}$	1
	$k_{\beta\alpha}^{f,2}$		$k_{\beta\alpha}^{b',2}$	$1/L_\alpha$	$k_{\beta\alpha}^{b,2}$	1
	$k_{\beta\beta}^{f,2}$		$k_{\beta\beta}^{b',2}$	$(L_\beta - 1)/L_\beta$	$k_{\beta\beta}^{b,2}$	1
	$k_{\alpha\beta}^{f,2}$		$k_{\alpha\beta}^{b',2}$	$1/L_\beta$	$k_{\alpha\beta}^{b,2}$	1

B. Domain lengths and rates at equilibrium

Given the rates in Table S1, we can solve the master equation (Eq. (5)) at equilibrium to obtain constraints on the equilibrium rates. At equilibrium, all currents are zero, which results in the following relations between the equilibrium rates and equilibrium domain lengths, $L_{\alpha,\text{eq}}$ and $L_{\beta,\text{eq}}$.

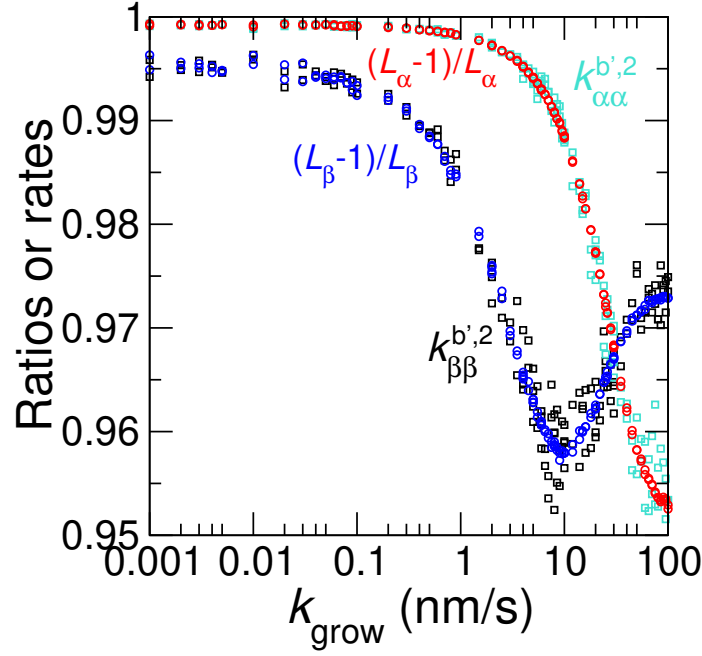


FIG. S1. Validation of the backward rate expressions used in the master equation. Domain lengths ratio $(L_\alpha - 1)/L_\alpha$ and $(L_\beta - 1)/L_\beta$ (blue and red circles) are computed from full bundle configurations in KMC simulations. The effective backward rates $k_{\alpha\alpha}^{b',2}$ (cyan) and $k_{\beta\beta}^{b',2}$ (black) in KMC simulations are computed as $k_{\alpha\alpha}^{b',2} = N_{\alpha\alpha}^{b,2}/N_{\alpha\alpha}^{b,2} + N_{\beta\alpha}^{b,2}$ and $k_{\beta\beta}^{b',2} = N_{\beta\beta}^{b,2}/N_{\alpha\beta}^{b,2} + N_{\beta\beta}^{b,2}$. $N_{ij}^{b,2}$ is the number of occurrences of unbinding the second head of an ABP, where i and j are the types of the last two ABPs at the tip.

$$\begin{aligned}
 k_{\alpha\alpha,eq}^{f,1} k_{\alpha\alpha,eq}^{f,2} &= \frac{L_{\alpha,eq} - 1}{L_{\alpha,eq}} \\
 k_{\beta\beta,eq}^{f,1} k_{\beta\beta,eq}^{f,2} &= \frac{L_{\beta,eq} - 1}{L_{\beta,eq}} \\
 k_{\alpha\beta,eq}^{f,1} k_{\alpha\beta,eq}^{f,2} k_{\beta\alpha,eq}^{f,1} k_{\beta\alpha,eq}^{f,2} &= \frac{1}{L_{\alpha,eq} L_{\beta,eq}}
 \end{aligned} \tag{S1}$$

Since the rate of binding of the first site does not depend on the filament separation, $k_{\alpha\alpha,eq}^{f,1} = k_{\beta\alpha,eq}^{f,1}$ and $k_{\beta\beta,eq}^{f,1} = k_{\alpha\beta,eq}^{f,1}$. Consequently, there are six independent forward rates at equilibrium. We use the constraints above but split the third equation in Eq. (S1) into the relations:

$$\begin{aligned}
 k_{\alpha\beta,eq}^{f,1} k_{\alpha\beta,eq}^{f,2} &= \frac{L_{\beta,eq} - 1}{L_{\beta,eq}(L_{\alpha,eq} - 1)} \\
 k_{\beta\alpha,eq}^{f,1} k_{\beta\alpha,eq}^{f,2} &= \frac{L_{\alpha,eq} - 1}{L_{\alpha,eq}(L_{\beta,eq} - 1)}.
 \end{aligned} \tag{S2}$$

An interpretation of Eq. (S2) is that the effective bending penalty in switching from α to β is $k_{\alpha\beta,eq}^{f,2}/k_{\beta\alpha,eq}^{f,2} = 1/(L_{\alpha,eq} - 1)$, and the bending penalty in switching from β to α is $k_{\beta\alpha,eq}^{f,2}/k_{\alpha\beta,eq}^{f,2} = 1/(L_{\beta,eq} - 1)$. We use these constraints on equilibrium rates to simplify the expression for the entropy production (see SI Section 4). Using Eq. (S1) and Eq. (S2), we are able to represent the equilibrium condition with four parameters, $L_{\alpha,eq}$, $L_{\beta,eq}$, $k_{\alpha\alpha,eq}^{f,1}$, and $k_{\beta\beta,eq}^{f,1}$.

C. Derivation of the self-consistency conditions

Under non-equilibrium conditions, the currents are non-zero. We need an additional constraint on the domain lengths to solve the master equation for L_α and L_β . For this purpose, we derive the following self-consistency

conditions, which are inspired by Ref. 35. We consider a chain of ABPs with the sequence of $\omega_l\omega_{l-1}\dots\omega_0$, where ω_i represents the type of ABP at position i , and the crosslinker at the tip is index $i = 0$. We write down an equation for the probability of finding this sequence at time t , $P^t(\omega_l\omega_{l-1}\dots\omega_0)$:

$$\begin{aligned} \frac{\partial P^t(\omega_l\omega_{l-1}\dots\omega_0)}{\partial t} &= w_{\omega_0|\omega_1}^+ P^t(\omega_l\omega_{l-1}\dots\omega_1) \\ &+ \sum_Z w_{Z|\omega_0}^- P^t(\omega_l|\omega_{l-1}\omega_{l-2}\dots\omega_0) P^t(\omega_{l-1}\omega_{l-2}\dots\omega_0|\omega_{l-2}\omega_{l-1}\dots\omega_0\omega_Z) P^t(\omega_{l-2}\omega_{l-1}\dots\omega_0\omega_Z) \\ &- (w_{\omega_0|\omega_1}^- + \sum_Z w_{Z|\omega_0}^+) P^t(\omega_l|\omega_{l-1}\omega_{l-2}\dots\omega_0) P^t(\omega_{l-1}\omega_{l-2}\dots\omega_0), \end{aligned} \quad (S3)$$

where $w_{\omega_i|\omega_j}^+$ is the rate of addition of ω_i to ω_j and $w_{\omega_i|\omega_j}^-$ is the rate of removal of ω_i to expose ω_j at the tip. In what follows, we solve Eq. (S3) at steady state:

$$\frac{\partial P^t(\omega_l\omega_{l-1}\omega_{l-2}\dots\omega_0)}{\partial t} = 0. \quad (S4)$$

We first substitute Eq. (S3) into Eq. (S4) and rearrange to express the possibility of having ω_l in addition to the sequence $\omega_{l-1}\omega_{l-2}\dots\omega_0$.

$$\begin{aligned} P^t(\omega_l|\omega_{l-1}\omega_{l-2}\dots\omega_0) &= \frac{w_{\omega_0|\omega_1}^+ P^t(\omega_l\omega_{l-1}\dots\omega_1)}{(w_{\omega_0|\omega_1}^- + v_{\omega_0}) P^t(\omega_{l-1}\omega_{l-2}\dots\omega_0)} \\ v_{\omega_0} &\equiv \frac{\sum_Z w_{Z|\omega_0}^+ P^t(\omega_{l-1}\omega_{l-2}\dots\omega_0) - \sum_Z w_{Z|\omega_0}^- P^t(\omega_{l-1}\omega_{l-2}\dots\omega_0\omega_Z)}{P^t(\omega_{l-1}\omega_{l-2}\dots\omega_0)} \end{aligned} \quad (S5)$$

Physically, v_{ω_0} is the growing rate at the tip with crosslinker type ω_0 . By further rearranging Eq. (S5) and summing over ω_0 , we obtain the following expression.

$$\sum_{\omega_0} w_{\omega_0|\omega_1}^+ P^t(\omega_l\omega_{l-1}\dots\omega_1) - \sum_{\omega_0} w_{\omega_0|\omega_1}^- P^t(\omega_l\omega_{l-1}\dots\omega_0) = \sum_{\omega_0} v_{\omega_0} P^t(\omega_l|\omega_{l-1}\omega_{l-2}\dots\omega_0) P^t(\omega_{l-1}\omega_{l-2}\dots\omega_0) \quad (S6)$$

The left side of Eq. (S6) is $v_{\omega_1} P^t(\omega_l\omega_{l-1}\dots\omega_1)$, so Eq. (S6) becomes

$$v_{\omega_1} P^t(\omega_l\omega_{l-1}\dots\omega_1) = \sum_{\omega_0} v_{\omega_0} P^t(\omega_{l-1}\omega_{l-2}\dots\omega_0) P^t(\omega_l|\omega_{l-1}\omega_{l-2}\dots\omega_0) \quad (S7)$$

Eq. (S7) is equivalent to Eq. 34 in ref. [35]. We use Γ_0 to represent the configuration $\omega_{l-1}\omega_{l-2}\dots\omega_0$ and Γ_1 to represent the configuration $\omega_l\omega_{l-2}\dots\omega_1$. Imagining that we focus on the configuration with a fixed length l from the tip of the chain ω_0 and moving backwards one position each time, Eq. (S7) provides a connection between the probability of finding Γ_1 and the probability of finding Γ_0 . We can write Eq. (S7) in matrix form as

$$P^t(\Gamma_1) = W(\Gamma_1|\Gamma_0) P^t(\Gamma_0) \quad (S8)$$

where $W(\Gamma_1|\Gamma_0) = P^t(\omega_l|\omega_{l-1}\omega_{l-2}\dots\omega_0)$ for consistent sequences Γ_0 and Γ_1 . Consequently, applying W N times, we have

$$P^t(\Gamma_N) = W^N P^t(\Gamma_0). \quad (S9)$$

At steady state, the eigenvector of W with eigenvalue 1 is the probability $\bar{P}(\Gamma)$ of finding a particular sequence Γ in the bulk. From Eq. (S7) we can now immediately see that

$$\bar{P}(\Gamma_\infty) = \frac{v_{tip}(\Gamma_\infty)}{\bar{v}} P^t(\Gamma_\infty), \quad (S10)$$

where Γ_∞ denotes a sequence in the bulk, \bar{v} is the total growth rate at the tip for all configurations, and $v_{tip}(\Gamma_i) = v_{\omega_i}$. In what follows, we use Eq. (S10) to derive the self-consistency conditions specific to our system. We choose two neighboring ABPs $\omega_m\omega_{m-1}$ for the configuration size, where m ranges from 1 to l . There are four configurations: $\omega_{m,\alpha}, \omega_{m-1,\alpha}, \omega_{m,\beta}, \omega_{m-1,\alpha}, \omega_{m,\alpha}, \omega_{m-1,\beta}$, and $\omega_{m,\beta}, \omega_{m-1,\beta}$. We refer to the term on the right hand side of Eq. (S10) as currents in the main text.

$$\begin{aligned}
v_{tip}(\omega_{m,\alpha}, \omega_{m-1,\alpha})P^t(\omega_{m,\alpha}, \omega_{m-1,\alpha}) &\equiv J_{\omega_{m,\alpha}, \omega_{m-1,\alpha}} \\
&= k_{\alpha\alpha}^{f,1}P(\alpha) - k_{\alpha\alpha}^{b,1}P(\alpha\alpha^*) = k_{\alpha\alpha}^{f,2}P(\alpha\alpha^*) - k_{\alpha\alpha}^{b,2}P(\alpha) \\
v_{tip}(\omega_{m,\beta}, \omega_{m-1,\beta})P^t(\omega_{m,\beta}, \omega_{m-1,\beta}) &\equiv J_{\omega_{m,\beta}, \omega_{m-1,\beta}} \\
&= k_{\beta\beta}^{f,1}P(\beta) - k_{\beta\beta}^{b,1}P(\beta\beta^*) = k_{\beta\beta}^{f,2}P(\beta\beta^*) - k_{\beta\beta}^{b,2}P(\beta) \\
v_{tip}(\omega_{m,\alpha}, \omega_{m-1,\beta})P^t(\omega_{m,\alpha}, \omega_{m-1,\beta}) &\equiv J_{\omega_{m,\alpha}, \omega_{m-1,\beta}} \\
&= k_{\alpha\beta}^{f,1}P(\alpha) - k_{\alpha\beta}^{b,1}P(\alpha\beta^*) = k_{\alpha\beta}^{f,2}P(\alpha\beta^*) - k_{\alpha\beta}^{b,2}P(\beta) \\
v_{tip}(\omega_{m,\beta}, \omega_{m-1,\alpha})P^t(\omega_{m,\beta}, \omega_{m-1,\alpha}) &\equiv J_{\omega_{m,\beta}, \omega_{m-1,\alpha}} \\
&= k_{\beta\alpha}^{f,1}P(\beta) - k_{\beta\alpha}^{b,1}P(\beta\alpha^*) = k_{\beta\alpha}^{f,2}P(\beta\alpha^*) - k_{\beta\alpha}^{b,2}P(\alpha)
\end{aligned} \tag{S11}$$

where $J_{\omega_{m,i}, \omega_{m-1,j}}$ is the current of ABPs of type j binding after ABPs of type i . J_{tot} is the sum of the four currents:

$$\bar{v} \equiv J_{\text{tot}} = J_{\omega_{m-1,\alpha}, \omega_{m,\alpha}} + J_{\omega_{m-1,\alpha}, \omega_{m,\beta}} + J_{\omega_{m-1,\beta}, \omega_{m,\beta}} + J_{\omega_{m-1,\beta}, \omega_{m,\alpha}}. \tag{S12}$$

By combining Eq. (S10) and Eq. (S11), we can obtain the following self-consistency condition,

$$\begin{aligned}
J_{\omega_{m-1,\alpha}, \omega_{m,\alpha}} &= \bar{P}^t(\omega_{m,\alpha}, \omega_{m-1,\alpha})J_{\text{tot}} \\
J_{\omega_{m-1,\beta}, \omega_{m,\beta}} &= \bar{P}^t(\omega_{m,\beta}, \omega_{m-1,\beta})J_{\text{tot}} \\
J_{\omega_{m-1,\alpha}, \omega_{m,\beta}} &= J_{\omega_{m-1,\beta}, \omega_{m,\alpha}} = \bar{P}^t(\omega_{m,\alpha}, \omega_{m-1,\beta})J_{\text{tot}}.
\end{aligned} \tag{S13}$$

The current $J_{\omega_{m-1,\alpha}, \omega_{m,\beta}}$ is identical to the current $J_{\omega_{m-1,\beta}, \omega_{m,\alpha}}$ because for every switch of a domain of α crosslinkers there is a switch to a domain of β crosslinkers. $\bar{P}^t(\omega_{m,\alpha}, \omega_{m-1,\alpha})$ is the probability of finding a specific configuration $\omega_m \omega_{m-1}$ in the bulk; it can be expressed in terms of the domain lengths as follows.

$$\begin{aligned}
\bar{P}^t(\omega_{m,\alpha}, \omega_{m-1,\alpha}) &= \frac{L_\alpha - 1}{L_\alpha + L_\beta} \\
\bar{P}^t(\omega_{m,\beta}, \omega_{m-1,\beta}) &= \frac{L_\beta - 1}{L_\alpha + L_\beta} \\
\bar{P}^t(\omega_{m,\alpha}, \omega_{m-1,\beta}) &= \bar{P}^t(\omega_{m,\beta}, \omega_{m-1,\alpha}) = \frac{1}{L_\alpha + L_\beta}
\end{aligned} \tag{S14}$$

Using Eq. (S13) and Eq. (S14), we obtain Eq. (6). Note that in main text we omit the ω 's in the subscripts of the currents for clarity. The self-consistency conditions are validated by KMC simulations (Fig. S2).

D. Domain lengths predicted by master equation

Since the equilibrium parameters and the driving parts of the rates are determined, we now use the self-consistency condition above to solve the master equation (Eq. (5)) for the domain lengths L_α and L_β under non-equilibrium conditions.

$$\begin{aligned}
L_\beta &= \frac{(L_\alpha - 1)k_{\beta\alpha}^{f,2} - k_{\alpha\alpha}^{f,2}(L_\alpha(k_{\beta\alpha}^{f,2} + 1)k_{\alpha\alpha}^{f,1} + L_\alpha - 1)}{k_{\beta\alpha}^{f,2}k_{\alpha\alpha}^{f,1}(Lk_{\alpha\alpha}^{f,2}((1 + k_{\alpha\beta}^{f,2})k_{\alpha\alpha}^{f,1} - (L_\alpha - 1)k_{\alpha\beta}^{f,2}k_{\beta\beta}^{f,1}) - (L_\alpha - 1)(1 + k_{\alpha\beta}^{f,2} + Lk_{\alpha\beta}^{f,2}k_{\beta\beta}^{f,1}))} \\
L_\alpha &= \frac{(L_\beta - 1)k_{\alpha\beta}^{f,2} - k_{\beta\beta}^{f,2}(L_\beta(k_{\alpha\beta}^{f,2} + 1)k_{\beta\beta}^{f,1} + L_\beta - 1)}{k_{\alpha\beta}^{f,2}k_{\beta\beta}^{f,1}(Sk_{\beta\beta}^{f,2}((1 + k_{\beta\alpha}^{f,2})k_{\beta\beta}^{f,1} - (L_\beta - 1)k_{\beta\alpha}^{f,2}k_{\alpha\alpha}^{f,1}) - (L_\beta - 1)(1 + k_{\beta\alpha}^{f,2} + Sk_{\beta\alpha}^{f,2}k_{\alpha\alpha}^{f,1}))}
\end{aligned} \tag{S15}$$

We compute the domain lengths from Eq. (S15) numerically and compare them with those measured from KMC simulations in Fig. 2. We solve Eq. (S15) using standard numerical routines in MATHEMATICA. The quality of the numerical solutions depends on the effectiveness of our mean field approach. In general, we find that the mean field approximations behind Eq. (S15) works well far from equilibrium but perform poorly close to equilibrium.

S3. DERIVATION OF EQ. (1)

In this section, we derive Eq. (1) of the main text. Our derivation closely follows those in Refs. 34 and 36. As in the main text, we focus of experimentally accessible currents J_α and J_β related to the net rate at which the different

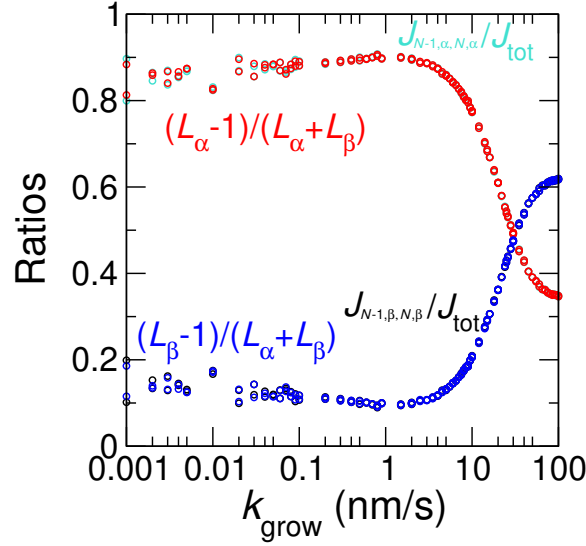


FIG. S2. Comparison of currents and domain length ratios from KMC simulations at various actin polymerization rates. Both currents and domain lengths are measured from KMC simulations of 10^6 steps. The simulation parameters are the same as those used in generating Fig. 2.

crosslinkers are assimilated into the bundle. In particular, using the notation in Fig. S3, we have

$$\begin{aligned} J_\alpha &= [j(1) + j(4) + j(5) + j(8)]/2 \\ J_\beta &= [j(2) + j(3) + j(6) + j(7)]/2, \end{aligned} \quad (\text{S16})$$

where we use $j(\epsilon)$ to denote the current along the edge ϵ .

Eq. (S16) can be written in matrix form as

$$J(n) = \sum_{\epsilon} j(\epsilon) d(\epsilon, n) \quad (\text{S17})$$

where $d(n, \epsilon)$ are elements in a matrix \mathbf{d} that describes how each of the generalized currents depends on the edge currents. For the specific case described above in Eq. (S16), the \mathbf{d} matrix can be written as:

$$\mathbf{d}^T = \frac{1}{2} \begin{pmatrix} 1 & 0 & 0 & 1 & 1 & 0 & 0 & 1 \\ 0 & 1 & 1 & 0 & 0 & 1 & 1 & 0 \end{pmatrix} \quad (\text{S18})$$

Before proceeding further, we outline the structure of the proof. We attempt to derive Eq. (1) by deriving constraints on the fluctuations of J_α and J_β (or equivalently $J(n)$ in Eq. (S17)). To do so we first express $J(n)$ in terms of the edge currents $\tilde{j}(\epsilon)$ such that $\tilde{j}(\epsilon)$ are guaranteed to satisfy current conservation, and they satisfy $J(n) = \sum_{\epsilon} \tilde{j}(\epsilon) d(\epsilon, n)$. Then, we use the findings of Ref. 34 which showed that the large deviation rate functions associated with the fluctuations in the various edge currents satisfy the following inequality,

$$I(\mathbf{j}) \leq \sum_{\epsilon} (j(\epsilon) - j^\pi(\epsilon))^2 \frac{\sigma^\pi(\epsilon)}{4[j(\epsilon)]^2}, \quad (\text{S19})$$

where $I(\mathbf{j})$ is the rate function of the edge currents and $\sigma^\pi(\epsilon)$ is the entropy production of edge ϵ . Finally, by writing Eq. (S19) in terms of the generalized currents $J(n)$, we obtain our central result.

We now proceed by first “inverting” Eq. (S17) and defining a set of edge currents:

$$\tilde{j}(\epsilon) = \sum_n J(n) G(n, \epsilon) \quad (\text{S20})$$

where \mathbf{G} is a pseudoinverse of the matrix \mathbf{d} . Note that since \mathbf{G} and \mathbf{d} are pseudoinverses of one another, we have

$$\sum_{\epsilon} \tilde{j}(\epsilon) d(\epsilon, k) = \sum_{n, \epsilon} J(n) G(n, \epsilon) d(\epsilon, k) = \sum_{n, \epsilon, \epsilon'} j(\epsilon') d(\epsilon', n) G(n, \epsilon) d(\epsilon, k) = \sum_{\epsilon'} j(\epsilon') d(\epsilon', k) = J(k) \quad (\text{S21})$$

If the set of currents $\tilde{\mathbf{j}}$ satisfy current conservation –we will construct a matrix \mathbf{G} below in Eq. S29 that satisfies this constraint –we can use the arguments in Ref. 34 and 36 to substitute Eq. (S20) into Eq. (S19) and obtain a bound on the large deviation rate function associated with the generalized currents, $I(\mathbf{J})$

$$I(\mathbf{J}) \leq \sum_{\epsilon} \left(\sum_n J(n)G(n, \epsilon) - J^\pi(\epsilon)G(n, \epsilon) \right)^2 \frac{\sigma^\pi(\epsilon)}{4[j(\epsilon)]^2}. \quad (\text{S22})$$

Now let's consider the system at steady state, with \mathbf{J}^π denoting the vector of average generalized currents and \mathbf{L} denoting the covariance of generalized currents. The rate function $I(\mathbf{J})$ can be expanded around the average generalized currents, \mathbf{J}^π , as

$$I(\mathbf{J}) \approx I(\mathbf{J}^\pi) + D[I(\mathbf{J})|\mathbf{J}^\pi] \cdot \tilde{\mathbf{J}} + \frac{1}{2} \tilde{\mathbf{J}}^T \cdot H[I(\mathbf{J})|\mathbf{J}^\pi] \cdot \tilde{\mathbf{J}} \quad (\text{S23})$$

Here $\tilde{\mathbf{J}}$ is a vector with elements $(J(n) - J^\pi(n))$, and $D[I(\mathbf{J})|\mathbf{J}^\pi]$ is the vector containing the derivatives of the rate function $I(\mathbf{J})$ with respect to the current \mathbf{J} . Since the rate function is at its minimum at \mathbf{J}^π , $I(\mathbf{J}^\pi)$ and $D[I(\mathbf{J})|\mathbf{J}^\pi]$ equal to 0. $H[I(\mathbf{J})|\mathbf{J}^\pi]$ is the Hessian matrix of $I(\mathbf{J})$ evaluated at \mathbf{J}^π which can be related to the covariance matrix \mathbf{L} by [44]

$$H[I(\mathbf{J})|\mathbf{J}^\pi] = \mathbf{L}^{-1}. \quad (\text{S24})$$

Eq. (S23) and Eq. (S24) then allow us to rewrite Eq. (S22) as

$$\tilde{\mathbf{J}}^T \cdot \mathbf{L}^{-1} \cdot \tilde{\mathbf{J}} \leq \tilde{\mathbf{J}}^T \cdot \mathbf{G} \mathbf{S} \mathbf{G} \cdot \tilde{\mathbf{J}} \quad (\text{S25})$$

Here \mathbf{G} is the matrix form of $G(n, \epsilon)$ with n indicating the row and ϵ indicating the column, \mathbf{G}^T is its transpose and \mathbf{S} is a diagonal matrix with elements $\sigma(\epsilon)/2|j(\epsilon)|^2$. Since Eq. (S22) is valid for any arbitrary fluctuation about the mean, $\mathbf{G} \mathbf{S} \mathbf{G}^T - \mathbf{L}^{-1}$ has to be positive semi-definite, which is to say that all of its eigenvalues have to be non-negative. For a 2×2 matrix, this is equivalent to

$$\text{Tr}(\mathbf{G} \mathbf{S} \mathbf{G}^T - \mathbf{L}^{-1}) \geq 0, \quad \text{Det}(\mathbf{G} \mathbf{S} \mathbf{G}^T - \mathbf{L}^{-1}) \geq 0. \quad (\text{S26})$$

To finish the proof, we now need to fix a matrix G . The choice of G is guided by the fact that the inequality in Eq. (S22) is only valid when the currents $\tilde{\mathbf{j}}$ are conserved currents, which means the sum of the currents that go through each node is zero. This gives the following constraints on the edge currents \tilde{j}_i (with the notation as specified in Fig. S3).

$$\tilde{j}(1) = \tilde{j}(5), \quad \tilde{j}(3) = \tilde{j}(7), \quad \tilde{j}(2) = \tilde{j}(4) = \tilde{j}(6) = \tilde{j}(8) \quad (\text{S27})$$

These constraints require that the elements in \mathbf{G} have the following relations.

$$G(i, 1) = G(i, 5), \quad G(i, 3) = G(i, 7), \quad G(i, 2) = G(i, 4) = G(i, 6) = G(i, 8) \quad (\text{S28})$$

where $i = 1$ or 2 are the first and second row of \mathbf{G} and represent the contributions of α and β components of the generalized currents to each edge currents.

The following \mathbf{G} matrix written in terms of L_α and L_β satisfies all the constraints and is also a psuedoinverse of the \mathbf{d} matrix:

$$\mathbf{G} = \frac{1}{(L_\alpha + L_\beta)} \begin{pmatrix} L_\alpha + L_\beta - 1 & 1 & -1 & 1 & L_\alpha + L_\beta - 1 & 1 & -1 & 1 \\ -1 & 1 & L_\alpha + L_\beta - 1 & 1 & -1 & 1 & L_\alpha + L_\beta - 1 & 1 \end{pmatrix} \quad (\text{S29})$$

Substituting the above equation into $\mathbf{G} \mathbf{S} \mathbf{G}^T$ and collecting the terms with $\ln dk_{\alpha/\beta}$ gives us the matrix $\delta\boldsymbol{\mu}$ in the main text. The rest is the matrix \mathbf{D} in main text.

S4. DERIVATION OF THE LINEAR RESPONSE LIKE IDENTITY

A fluctuation dissipation like form can also be obtained as in Eq. (13) of the main text. In this section, we derive Eq. (13) using the matrix $\mathbf{G} \mathbf{S} \mathbf{G}^T$ we determined in Section S3. First, we multiply the matrix $\mathbf{G} \mathbf{S} \mathbf{G}^T$ by the vector \mathbf{J} on both sides:

$$\mathbf{J}^T \mathbf{G} \mathbf{S} \mathbf{G}^T \mathbf{J} = \mathbf{j}^T \mathbf{S} \mathbf{j} = \dot{\sigma}/2 \quad (\text{S30})$$

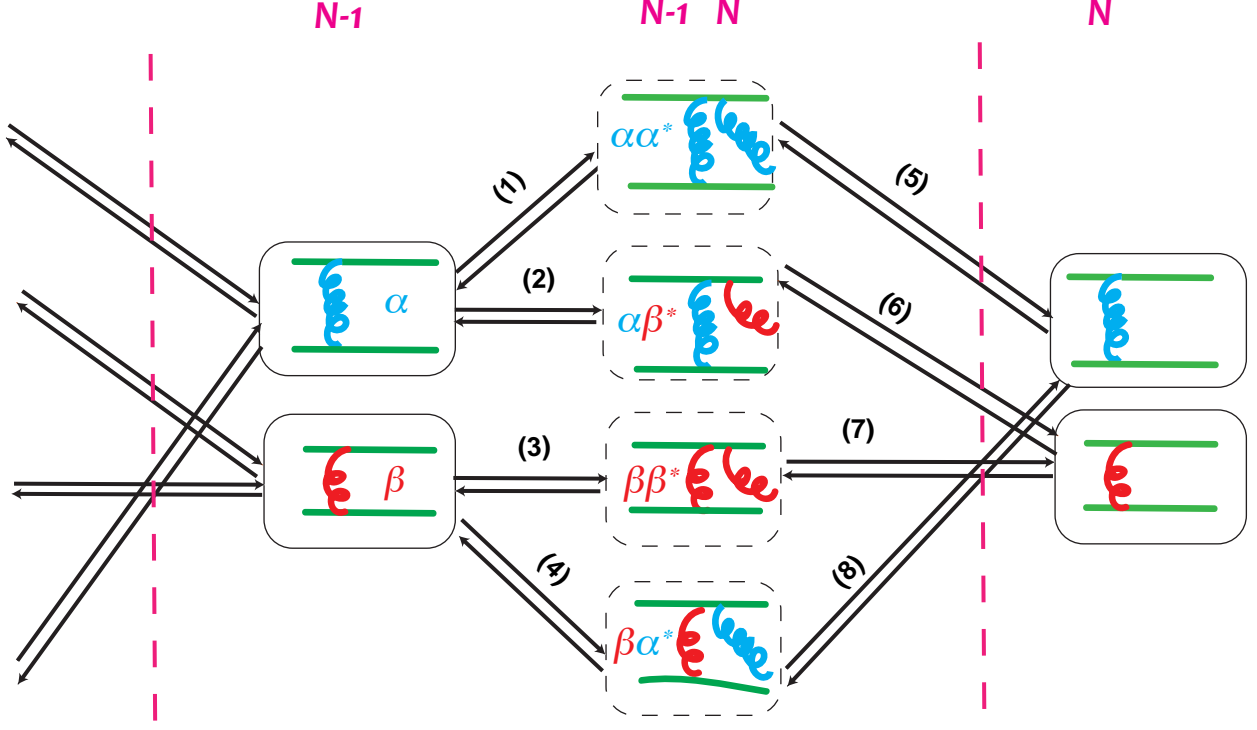


FIG. S3. Schematic showing all the possible transitions of the actin bundle system. We index the graph edges from 1 to 8.

With $\mathbf{J}^T = (J_\alpha, J_\beta)$ and $\mathbf{j}^T = (j_1, j_2, \dots, j_8)$ The entropy production can be further rewritten as:

$$\dot{\sigma} = J_{\text{tot}}(\Delta\mu - \varepsilon_{\text{diss}}) = 2\mathbf{J}^T (\mathbf{dk} - \mathbf{D}[\mathbf{p}]) \quad (\text{S31})$$

where the microscopic force vector \mathbf{dk} and the relative entropy term $\mathbf{D}[\mathbf{p}]$ are defined as

$$\mathbf{dk} = \begin{pmatrix} \log dk_\alpha \\ \log dk_\beta \end{pmatrix} \quad (\text{S32})$$

$$\mathbf{D}[\mathbf{p}] = \begin{pmatrix} D(P(\alpha)||P^{\text{eq}}(\alpha)) \\ D(P(\beta)||P^{\text{eq}}(\beta)) \end{pmatrix}$$

with

$$D(P(i)||P^{\text{eq}}(i)) = \frac{L_i - 1}{2L_i} \left(\log \frac{L_i - 1}{L_i} - \log \frac{L_{i,\text{eq}} - 1}{L_{i,\text{eq}}} \right) + \frac{1}{2L_i} \left(\log \frac{1}{L_i} - \log \frac{1}{L_{i,\text{eq}}} \right) \quad (\text{S33})$$

We then arrive at:

$$\mathbf{J}^T \mathbf{G} \mathbf{S} \mathbf{G}^T \mathbf{J} = \mathbf{J}^T (\delta\boldsymbol{\mu} - \mathbf{D}) \mathbf{J} = \mathbf{J}^T (\mathbf{dk} - \mathbf{D}[\mathbf{p}]) \quad (\text{S34})$$

So when $\delta\boldsymbol{\mu} - \mathbf{D} = \mathbf{L}^{-1}$, we obtain Eq. (13) in the main text.

S5. THE THERMODYNAMIC BOUND FOR DRIVING IS IMPROVED BY CONSIDERING INDIVIDUAL CURRENTS INSTEAD OF THE TOTAL CURRENT IN THE TUR

We use Eq. (S12) to re-write Eq. (7):

$$\dot{\sigma} = J_{\text{tot}} \left(\frac{L_\alpha - 1}{L_\alpha + L_\beta} \log \frac{k_{\alpha\alpha}^{f,1} k_{\alpha\alpha}^{f,2}}{k_{\alpha\alpha}^{b,1} k_{\alpha\alpha}^{b,2}} + \frac{L_\beta - 1}{L_\alpha + L_\beta} \log \frac{k_{\beta\beta}^{f,1} k_{\beta\beta}^{f,2}}{k_{\beta\beta}^{b,1} k_{\beta\beta}^{b,2}} + \frac{1}{L_\alpha + L_\beta} \log \frac{k_{\alpha\beta}^{f,1} k_{\alpha\beta}^{f,2} k_{\beta\alpha}^{f,1} k_{\beta\alpha}^{f,2}}{k_{\beta\beta}^{b,1} k_{\beta\beta}^{b,2} k_{\beta\alpha}^{b,1} k_{\beta\alpha}^{b,2}} \right) \quad (\text{S35})$$

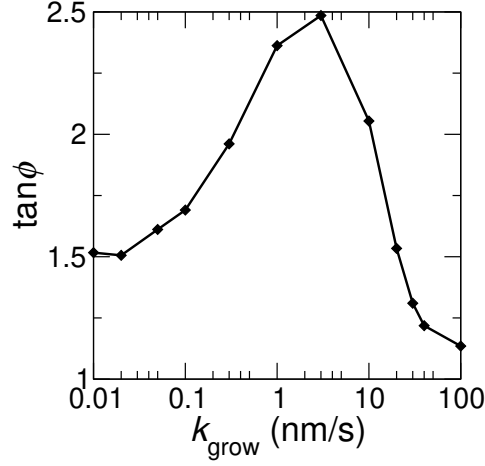


FIG. S4. Coefficient $\tan \phi$ at various actin polymerization rates k_{grow} . The parameters are the same as in Fig. 5.

We combine Eqs. (S1), (S2), (S35) and (S36) to obtain the following expression for entropy production in terms of $\Delta\mu$ and $\varepsilon_{\text{diss}}$ in Eq. (8) and Eq. (9)

$$\dot{\sigma} = J_{\text{tot}}(\Delta\mu - \varepsilon_{\text{diss}}) \quad (\text{S36})$$

We first plot the second law bound and the TUR bound (Eq. (15)) in Fig. 5. The TUR bound is much better than the second law bound because it encodes the kinetic information of the process. It deviates from the real driving at intermediate polymerization rate $k_{\text{grow}} = 1$ nm/s. For further improvement, we can adapt the MTUR bound [37] to this process. We define the fluxes of adding α and β ABPs as $J_{\alpha} = J_{\omega_{m-1,\alpha},\omega_{m,\alpha}} + J_{\omega_{m-1,\beta},\omega_{m,\alpha}}$ and $J_{\beta} = J_{\omega_{m-1,\alpha},\omega_{m,\beta}} + J_{\omega_{m-1,\beta},\omega_{m,\beta}}$. The MTUR bound given by Eq. (14) is the same as considering the scalar observable $J_{\text{tot}'} = \cos \phi J_{\alpha} + \sin \phi J_{\beta}$ and then maximizing $2 \langle J_{\text{tot}'}^2 \rangle / t J_{\text{tot}} \langle \delta J_{\text{tot}'}^2 \rangle$ by varying ϕ . We demonstrate below the derivation and plot the $\tan \phi$ values that optimize the bound as a function of k_{grow} .

Inserting the expression of $J_{\text{tot}'}$ into the bound of $2 \langle J_{\text{tot}'}^2 \rangle / t J_{\text{tot}} \langle \delta J_{\text{tot}'}^2 \rangle$, we obtain

$$\Delta\mu \geq \varepsilon_{\text{diss}} + \frac{2(J_{\alpha} + \tan \phi J_{\beta})^2}{t J_{\text{tot}} (\langle \delta J_{\alpha}^2 \rangle + \tan^2 \phi \langle \delta J_{\beta}^2 \rangle + 2 \tan \phi \langle \delta J_{\alpha} \delta J_{\beta} \rangle)} \quad (\text{S37})$$

We take the derivative of Eq. (S37) against $\tan \phi$ and find that the maximum value is achieved when

$$\tan \phi = \frac{-\langle \delta J_{\alpha} \delta J_{\beta} \rangle J_{\alpha} + \langle \delta J_{\alpha}^2 \rangle J_{\beta}}{-\langle \delta J_{\alpha} \delta J_{\beta} \rangle J_{\beta} + \langle \delta J_{\beta}^2 \rangle J_{\alpha}}. \quad (\text{S38})$$

We substitute Eq. (S38) for $\tan \phi$ in Eq. (S37) and obtain the following MTUR bound for the bundling process.

$$\Delta\mu \geq \varepsilon_{\text{diss}} + \frac{2(J_{\alpha}^2 \langle \delta J_{\beta}^2 \rangle - 2 \langle \delta J_{\alpha} \delta J_{\beta} \rangle J_{\alpha} J_{\beta} + J_{\beta}^2 \langle \delta J_{\alpha}^2 \rangle)}{t J_{\text{tot}} (-\langle \delta J_{\alpha} \delta J_{\beta} \rangle^2 + \langle \delta J_{\alpha}^2 \rangle \langle \delta J_{\beta}^2 \rangle)}. \quad (\text{S39})$$

This is equivalent to Eq. (14), where we simplify the expression using

$$\mathbf{J} = \begin{pmatrix} J_{\alpha} \\ J_{\beta} \end{pmatrix}, \mathbf{dk} = \begin{pmatrix} \log dk_{\alpha} \\ \log dk_{\beta} \end{pmatrix} \text{ and } \mathbf{D}[\mathbf{p}] = \begin{pmatrix} D(P(\alpha) || P^{eq}(\alpha)) \\ D(P(\beta) || P^{eq}(\beta)) \end{pmatrix}. \quad (\text{S40})$$

Fig. S4 shows the value of $\tan \phi$ in Eq. (S38) at various k_{grow} . This coefficient is obtained by maximizing the bound in Eq. (S37) at each data point. It provides information about the strength of the correlation between the two currents. We compare this bound with the one given by the TUR (Eq. (15)) in Fig. 5 and discuss their performance in the main text.

To further analyze how the variance and covariance of fluxes modulate the value of $\tan \phi$ and the amount of driving used to maintain the correlation between fluxes, we rearrange the expression of $\tan \phi$ as follows.

$$\tan \phi = \frac{J_{\alpha}}{J_{\beta}} \left[\frac{-\langle \delta J_{\alpha} \delta J_{\beta} \rangle}{J_{\alpha} J_{\beta}} + \frac{\langle \delta J_{\alpha}^2 \rangle}{J_{\alpha}^2} \right] \quad (\text{S41})$$

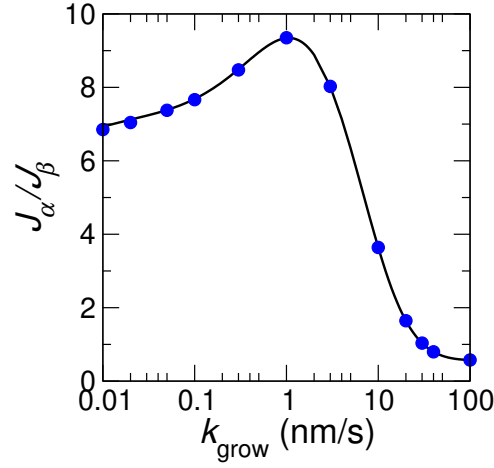


FIG. S5. The ratio between the two currents J_α/J_β computed from KMC simulations (blue points) and predicted by the master equation (black curve).

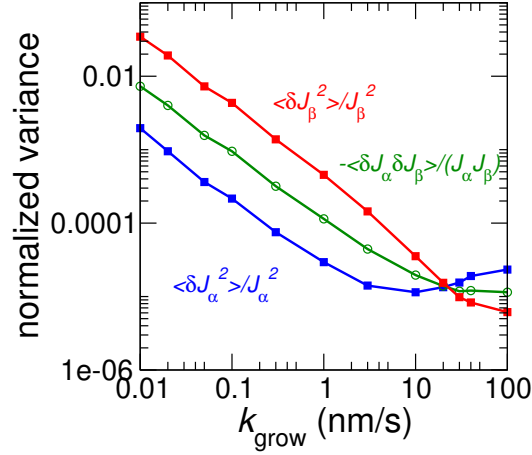


FIG. S6. Normalized variance and covariance computed from KMC simulations. Blue and red points are the variance normalized by the corresponding current ($\langle \delta J_\beta^2 \rangle / J_\beta^2$ and $\langle \delta J_\alpha^2 \rangle / J_\alpha^2$) computed from simulations. Green points are the covariance normalized by the magnitude of the two currents ($-\langle \delta J_\alpha \delta J_\beta \rangle / J_\alpha J_\beta$).

Fig. S4 shows that the ratio between currents J_α/J_β has the same non-monotonic dependence on actin polymerization rate as $\tan \phi$. This is consistent with Eq. (S41). On the other hand, the normalized variance and covariance of currents $-\langle \delta J_\alpha \delta J_\beta \rangle / J_\alpha J_\beta$, $\langle \delta J_\alpha^2 \rangle / J_\alpha^2$ and $\langle \delta J_\beta^2 \rangle / J_\beta^2$ have similar orders of magnitude for a given k_{grow} (Fig. S6), suggesting that the value of $\tan \phi$ is weakly dependent on the second term on the right side of Eq. (S41). We conclude that $\tan \phi$, as well as the strength of the correlation between fluxes is mainly determined by the ratio between the two currents.